Gulf Stream Moisture Fluxes Impact Atmospheric Blocks Throughout the Northern Hemisphere

J. P. Mathews[1], A. Czaja[1], F. Vitart[2], and C. Roberts[2]

[1]Imperial College London
[2]European Centre for Medium-Range Weather Forecasts

Key Points:

- Gulf Stream moisture flux suppression reduces atmospheric blocking across the northern hemisphere.
- Gulf Stream moisture fluxes generate larger jet stream perturbations, fostering faster westward-propagating Rossby waves.
- Higher resolution models enhance signal transport from the boundary layer to the upper troposphere.

Corresponding author: Jamie Mathews, `jamie.mathews19@imperial.ac.uk`

Abstract

In this study, we explore the impact of oceanic moisture fluxes on atmospheric blocks using the ECMWF Integrated Forecast System. Artificially suppressing surface latent heat flux over the Gulf Stream region leads to a significant reduction (up to 30%) in atmospheric blocking frequency across the northern hemisphere. Affected blocks show a shorter lifespan (-6%), smaller spatial extent (-12%), and reduced intensity (-0.4%), with an increased detection rate (+17%). These findings are robust across various blocking detection thresholds. Analysis indicates a resolution-dependent response, with resolutions lower than Tco639 (∼18km) showing no significant change in some blocking characteristics, even with reduced blocking frequency. Exploring the broader Rossby wave pattern, we observe that diminished moisture flux favours eastward propagation and higher zonal wavenumbers, while air-sea interactions promotes stationary and westward-propagating waves with zonal wavenumber 3. This study underscores the critical role of western boundary current's moisture fluxes in modulating atmospheric blocking.

1 Introduction

Understanding the mechanisms governing the formation and persistence of large-scale anticyclonic anomalies, commonly known as atmospheric blocks, is crucial for advancements in weather forecasting (Grams et al., 2018) and predicting the associated extreme temperatures (Pfahl & Wernli, 2012). Nearly a decade ago, Pfahl et al. (2015) linked these synoptic-scale features to upstream latent heating, an observation later substantiated by Steinfeld et al. (2020). Their experiment, suppressing latent heating along the warm conveyor belt of a cyclone, resulted in the subsequent suppression of atmospheric blocks, with some blocks failing to form at all within the 10-day simulations.

The ocean's role as a primary moisture source for atmospheric blocks was highlighted by Yamamoto et al. (2021), with theories by Mathews and Czaja (2024) suggesting that western boundary currents, like the Gulf Stream, modulate atmospheric blocking. This link was evidenced by increased blocking following heightened Gulf Stream heat transport, leading to warm water anomalies that boost surface latent heat flux (SLHF) and, consequently, moisture aiding block formation by transferring low potential vorticity (PV) air from lower to upper levels (Wenta et al., 2024).

Emphasis has also been placed on both oceanic and atmospheric resolution to accurately represent air-sea interactions in coupled models (Hewitt et al., 2017). Notably, Paolini et al. (2021) found that models with atmospheric resolution coarser than 50km exhibited an entirely different response to sea surface temperature anomalies, showing weakened vertical motion and meridional transient eddy heat transport. The impact this had on atmospheric blocking increased with higher atmospheric resolutions.
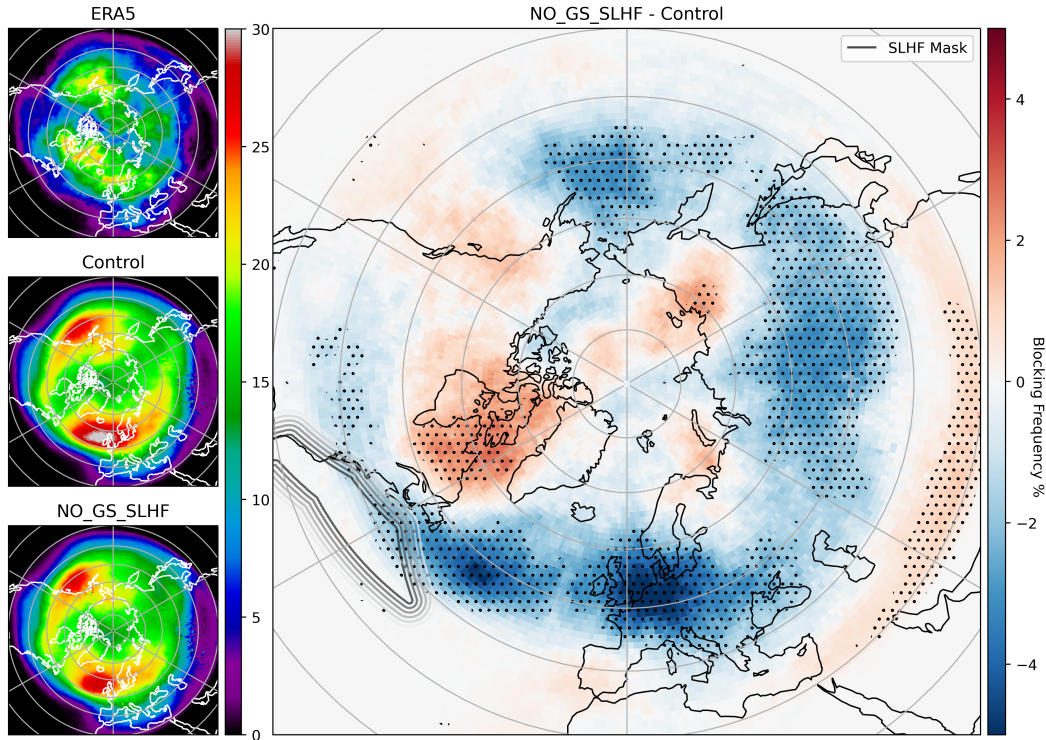
In this study, we investigate the effect of moisture fluxes from the Gulf Stream region on atmospheric blocking in the northern hemisphere (NH) using the state-of-the-art European Centre for Medium-Range Weather Forecasts (ECMWF) Integrated Forecast System (IFS). While this study emphasises changes in atmospheric blocks, we also examine the effect on the broader Rossby wave spectrum, as previously done by Randel and Held (1991). The paper is laid out as follows: Section 2 describes the model setup and the diagnostic methods used. Section 3 shows the effects Gulf Stream moisture suppression has on the upper troposphere, followed by our conclusions in Section 4.

2 Data and Methodology

2.1 Model Set Up

The results in this study are based on coupled ensemble reforecasts using the ECMWF IFS cycle 47r3 (ECMWF, 2023), configured as follows. The atmosphere is set up with

15 ensemble members, 137 model levels and run on Tco639, Tco319, and Tco199 cubic octahedral reduced Gaussian grids, corresponding to resolutions of approximately 18km, 32km, and 50km, respectively. The IFS is coupled hourly to a 75-level NEMO v3.4 ocean model (Madec et al., 2017) and an LIM2 sea ice model (Bouillon et al., 2009; Fichefet & Maqueda, 1997), both utilising the ORCA025 tripolar grid with a grid spacing of approximately 0.25°. The ocean and atmosphere are fully coupled throughout the 46-day forecast, producing output every 12 hours. Fifteen reforecasts are used, and the initial dates are listed in the Supplementary Table 1. The atmospheric, land, and wave fields were initialised from ERA5 (Hersbach et al., 2020), while the ocean and sea ice fields were initialised from OCEAN5 and ORAS5 respectively (Zuo et al., 2019). These dates were chosen based on the occurrence of a cyclone over the North Atlantic preceding the initial block detected in the North Atlantic or Europe region, as observed from ERA5 data. The forecast was initiated approximately 4 days before the observed block was initially detected to allow the contributing cyclone to sufficiently interact with the Gulf Stream. These events were chosen randomly, excluding the 2010 British Isles cold spell, the 2019 European heatwave, and the 2022 European cold spell, with priority given to more recent dates due to higher-quality data assimilation (de Rosnay et al., 2022). All results shown are for resolution Tco639 unless otherwise specified.

Figure 1. Mean blocking frequency for ERA5 (top left), the control run (middle left), the NO_GS_SLHF run (bottom left), and the difference between the NO_GS_SLHF and control runs (right). The grey contours indicate the SLHF mask applied, with the darkest (lightest) contour indicating complete suppression (permission). Stippling indicates areas that exceed the 95% confidence interval.

To assess the impact of Gulf Stream (GS) SLHF on atmospheric blocking, a sensitivity experiment was conducted. It compared the full physics control run to a corresponding simulation with GS SLHF suppressed (here-after referred to as NO_GS_SLHF).

GS SLHF is turned off by applying a mask to the moisture transfer scheme (ECMWF, 2021), preventing moisture transfer where the mask is applied. This mask linearly relaxed, allowing complete moisture transfer after a distance of 5° from the original mask, as illustrated by the grey contours in Fig. 1. The mask roughly corresponds to the region of 200Wm^{-2} SLHF from wintertime ERA5 climatology in the North Atlantic and was applied throughout the entire run.

2.2 Diagnostic Methods

Following Schwierz et al. (2004), blocking is identified as an upper-level negative PV anomaly that surpasses defined thresholds for overlap, amplitude, spatial scale, and duration. Initially, the PV field is averaged between 500hPa and 150hPa, and a two-day running average is applied. To calculate the anomaly, a two-day smoothed daily ERA5 climatology is subtracted from the averaged PV field. The upper PV anomaly field is then analysed using the Steinfeld (2020) algorithm, with thresholds for overlap, duration, amplitude, and size being 40%, 5 days, -1.2PVU and 10^6km^2 respectively. The relatively low overlap threshold is chosen due to the 12-hourly temporal output from the model and to maximise the difference between the NO_GS_SLHF and control runs. Various threshold values were tested, and most results were comparable across different overlap and amplitude thresholds, as discussed in Section 3.3. Each detected block is labelled, and its characteristics, including duration, size, and intensity (total PV per area), are calculated for each time step. These characteristics are related to the overall blocking frequency in the NH, as seen in Table 1, through the equations:

$$\text{Frequency}(x,y) = \frac{1}{TDM} \sum_{t=1}^{T} \sum_{d=1}^{D} \sum_{m=1}^{M} f(x,y,t,d,m), \tag{1}$$

$$f(x,y,t,d,m) = \begin{cases} 1, & \text{if blocking is detected at grid point} \\ 0, & \text{otherwise} \end{cases}, \tag{2}$$

$$\iint_{NH} \text{Frequency}(x,y)\, dxdy = \frac{\sum_{n=1}^{N} \text{Duration} \times \overline{\text{Size}}}{\text{Forecast Length}}, \tag{3}$$

where T, D, M, and N represent the number of time steps, initial dates (as seen in Supplementary Table 1), ensemble members, and blocks detected, respectively. The overbar denotes the average over the life cycle of the block.

The phase speed - wavenumber analysis is conducted following Jiménez-Esteve et al. (2022). First, an area-weighted latitudinal mean between 40°N and 60°N is computed using the same upper PV anomaly field used for blocking detection. A fast Fourier transform is then applied in the longitudinal direction. The phase speed of the Rossby waves is calculated as per Randel and Held (1991).

Statistical significance at the 95% confidence interval is determined using a two-tailed t-test between the ensemble members of the NO_GS_SLHF and control runs.
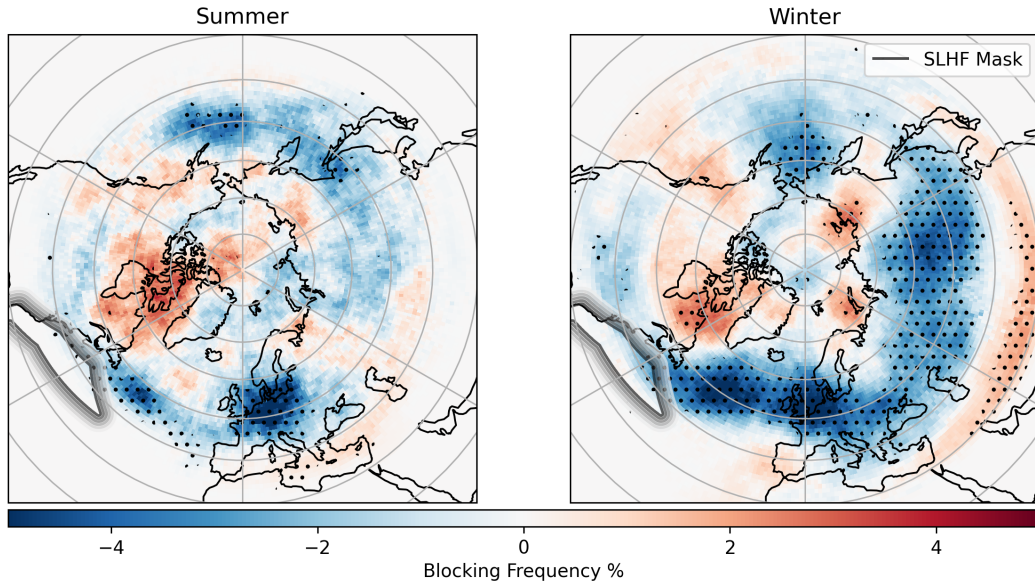
3 Results

3.1 The Effect on Atmospheric Blocking

Fig. 1 compares average blocking frequencies from ERA5 data, control, and NO_GS_SLHF simulations over a 46-day forecast. Both simulations show a more extensive frequency of atmospheric blocking across the Northern Hemisphere than observed in ERA5, with

a smoother signal attributed to ensemble spread. The NO_GS_SLHF simulation reveals a significant decrease in blocking frequency, by up to 30%, over the North Atlantic storm track, Western Europe, Russia, and the North Pacific compared to the control, as high-lighted in the right panel of Fig. 1. Conversely, it shows an increase in blocking over north-eastern Canada and central Asia, though with a smaller spatial footprint and intensity, suggesting a complex shift in blocking patterns.

Table 1. Percentage change in blocking frequency over the NH relative to the control run for the entire reforecast period is presented. The first two weeks of the forecast are shown in brackets. Winter reforecasts correspond to NDJFMA, while Summer corresponds to MJJASO, as indicated in Supplementary Table 1. Results significant over the 99% confidence interval are depicted in **bold**.

Resolution	All Dates	Winter	Summer
Tco639	**-4.34% (-4.22%)**	**-5.9% (-6.64%)**	**-2.45%** (-1.33%)
Tco319	**-3.88% (-2.96%)**	**-5.32% (-4.90%)**	**-2.60%** (-0.18%)
Tco199	**-3.35% (-3.55%)**	-3.30% (**-5.27%**)	**-3.41%** (-1.51%)

Results from the first two weeks of reforecasts align more closely with ERA5 (Supplementary Fig. 1), indicating a significant decrease in blocking over the North Atlantic and Western Europe. This suggests that the signal has not had sufficient time to propagate, either directly through advection (Yamamoto et al., 2021) or indirectly via jet stream resonance (Coumou et al., 2014; He et al., 2023), to the other oceanic basin. An overall reduction of 4.22% in Northern Hemisphere blocking frequency for this period was observed, as detailed in Table 1.
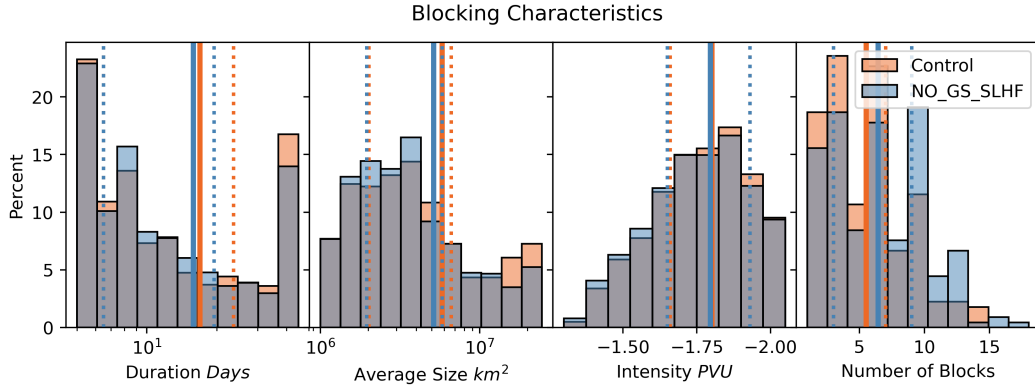

Figure 2. The difference in mean blocking frequency between the NO_GS_SLHF and control runs for the extended summer (left) and extended winter (right). The grey contours indicate the SLHF mask applied, with the darkest (lightest) contour indicating complete suppression (permission). Stippling indicates areas that exceed the 95% confidence interval.

Turning to the seasonal strength of this signal, the same analysis was conducted for dates within the extended winter (NDJFMA) and extended summer (MJJASO) periods, as indicated in Supplementary Table 1. The results of this seasonal analysis are presented in Fig. 2. The summer composite reveals a significant decrease in blocking over the North Atlantic storm track, Western Europe, Northern Japan, and the North Pacific. Additionally, during winter, a more prominent area of reduced blocking spans from the Western North Atlantic to East Asia, accompanied by a signal in the North Pacific. Notably, only the extended winter period exhibits the same spatial increases in blocking frequency as depicted in Fig. 1. Expanding this perspective to encompass the overall change in blocking frequency across the NH, once more, the dominance of the signal in extended winter becomes evident, as displayed in Table 1.

Examining the changes in the atmospheric block's characteristics reveals the impact of air-sea interactions on individual blocks. Figure 3 shows the probability distributions of these characteristics. The solid line, representing the mean value, illustrates that in the NO_GS_SLHF run, the blocks have shorter life cycles, a more compact spatial signature, and exhibit weaker intensity, indicating a weaker negative PV anomaly inside the blocks. Interestingly, the NO_GS_SLHF run detects more individual blocks compared to the control run. However, due to their decreased duration and size, this discrepancy is not substantial enough to result in an overall increase in blocking frequency, as indicated in Table 1 and seen in Fig. 1 and 2. The dotted lines in Fig. 3 illustrate the upper and lower quartiles of the distribution. This demonstrates that in the NO_GS_SLHF run, there is a narrower range of block durations and sizes, indicating reduced variability. Conversely, the NO_GS_SLHF run demonstrates wider variability in terms of the number of individual blocks detected and their respective intensities.
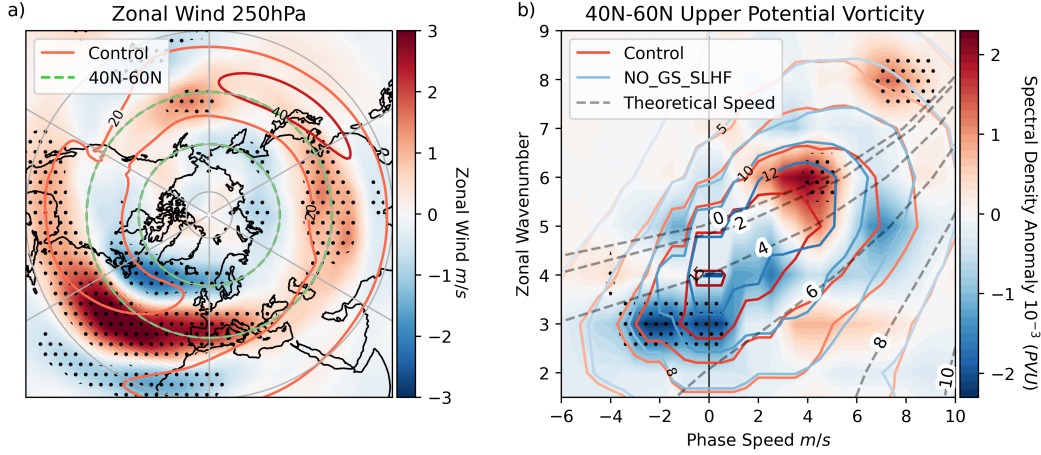

Figure 3. The distributions of the block characteristics for the control (light red) and NO_GS_SLHF (light blue) runs. From left to right the block's duration, average size, intensity (total PV per area), and the number of individual blocks detected per forecast are shown. Solid lines represent the mean values, while dotted lines represent the upper quartiles.

3.2 Changes in the Jet Stream and Rossby Wave Characteristics

Examining the overall change in the jet stream due to suppressed GS SLHF reveals a signal across the NH. Figure 4a illustrates the difference in the zonal wind at 250hPa between the NO_GS_SLHF and control runs, with the average zonal wind for the control run depicted with the red contours. In the North Atlantic, an equatorward shift is seen in the eddy-driven jet, while a poleward shift is seen in the subtropical jet, suggestive of a merged jet. Further downstream over central Asia and the North Pacific, there

163 are signs of a poleward shift in the jet. Additionally, there is a more general increase in
164 jet speed over the North Pacific that aligns with the decrease in atmospheric blocking
165 seen in Figs. 1 and 2. This is in line with the links between zonal wind and atmospheric
166 blocking seen by Riboldi et al. (2020). While there is a small but significant increase in
167 the zonal wind above the 95% confidence interval for the entire NH of 0.9% in the NO_GS_SLHF
168 run, there is no dipole signal when averaging above and below the jet stream maximum,
169 suggestive of no overall meridional shift in the jet stream. This result is also confirmed
170 by meridional cross sectional composites (Supplementary Fig. 2).

Figure 4. The zonal wind at 250hPa (a) and the power spectrum of the vertically averaged anomalous PV field from 500hPa to 150hPa within the latitudinal range of 40°N to 60°N (b) are presented. In both figures, the shading illustrates the difference between the NO_GS_SLHF and control runs, with the blue and red contours representing their respective reforecast means. The region between 40°N and 60°N is indicated by green dashed lines. The theoretical phase speed for different meridional wavenumbers at 40°N, applying a background flow of 16.4 m/s as observed, is depicted with grey dashed lines. Areas that exceed the 95% confidence interval are highlighted with stippling.

171 Analysing the centre of mass of the blocks to infer any stationary differences be-
172 comes challenging due to the merging and splitting of negative PV anomaly air masses
173 (Hauser et al., 2023). However, a spectral-based approach proves more effective. Fig. 4b
174 presents the power spectrum of the vertically averaged anomalous PV field from 500hPa
175 to 150hPa, spanning the latitudinal range of 40°N to 60°N. The contours depict the spec-
176 tral density of the NO_GS_SLHF (blue) and control runs (red), while the shading shows
177 the difference between the two. This figure illustrates that both the NO_GS_SLHF and
178 control runs exhibit faster westward propagation with decreasing zonal wave number.
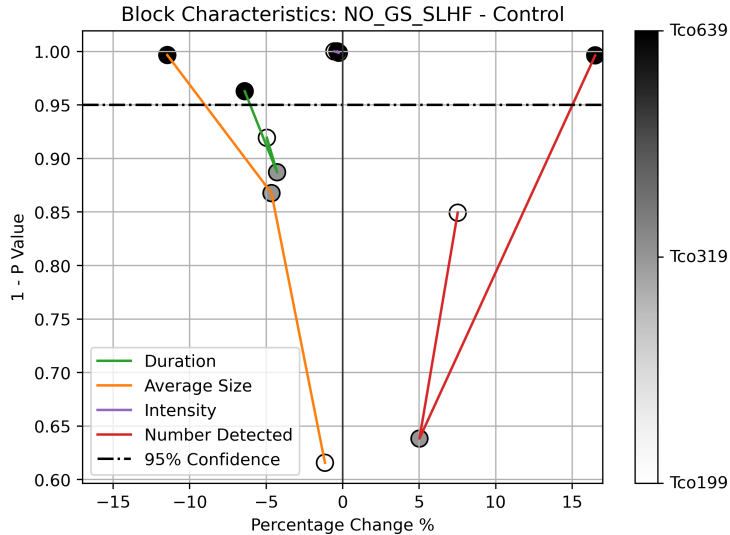
179 Comparing the differences between the two, the NO_GS_SLHF runs exhibit a more
180 pronounced inclination toward higher wavenumbers, facilitating faster eastward prop-
181 agation. Conversely, the control run displays a preference for westward and stationary
182 zonal waves characterised by lower wavenumbers. There is no significant change in the
183 average zonal wind between 40N-60N, and hence we can deduce that this signal is not
184 due to a change in jet speed but a result of suppressed Rossby wave forcing. This ob-
185 served distinction aligns with expectations, considering the increased blocking size in the
186 control run, as seen in Fig. 3, and again agrees with the observations of Riboldi et al.
187 (2020) linking low phase speed with atmospheric blocking.

Examining the seasonal change in this signal (Supplementary Fig. 3), the power spectrum shifts from primarily exhibiting wavenumbers 4-7 in summer to 3-5 in winter. Additionally, the most pronounced stationary wave changes from zonal wavenumber 4 in summer to wavenumber 3 in winter, consistent with the increased zonal wind observed during winter. Furthermore, the difference between the NO_GS_SLHF and control runs shifts from the dipole signature seen in Fig. 4b in summer to an overall reduction of wavenumbers 3-5 in winter. This again underscores the comparatively strong signal exerted by air-sea interactions in winter compared to summer. We now compare the difference between model resolutions.

3.3 Dependence on Model Resolution

Firstly, examining the change in blocking frequency, Table 1 illustrates the variation in blocking frequency between the NO_GS_SLHF and control runs for the entire NH. While this reveals a significant decrease in blocking frequency for the entire run across all resolutions, the strength of this signal diminishes with decreased resolution. However, this trend is not consistent when considering only the first two weeks of the forecast, although Tco639 still exhibits the most substantial change. Surprisingly, the opposite is true when focusing solely on summer dates, with lower resolutions showing a larger difference between the two runs.

Analysing the change in blocking frequency for lower resolutions (Supplementary Fig. 4 and Fig. 5) a smaller spatial signature is observed in both lower resolution runs, neither of which propagates to the North Pacific. The Tco199 run has the largest spatial signature among the lower resolution runs, albeit with a considerably weaker magnitude. All three resolutions show an increase in blocking over Northeastern Canada, which shifts westward with lower resolution.

Figure 5. The percentage change in the block's characteristics for the NO_GS_SLHF run with respect to the control run for all resolutions. The block's duration, average size, intensity, and the number of individual blocks detected per forecast are shown in green, orange, purple, and red, respectively. The darkest dots indicate the highest resolution. The dashed black line indicates the 95% confidence level.

Fig. 5 displays the percentage change in atmospheric blocking characteristics versus the significance of this result, with higher model resolution depicted with darker dots. This figure reaffirms that, across all resolutions, when GS SLHF is suppressed, blocks exhibit a shorter duration, are spatially smaller, and have weaker intensity, though more individual blocks are detected. Importantly, this signal is significant at the 95% confidence interval (above the dashed line) only for the highest resolution, Tco639, excluding the change in intensity. Lower resolutions show a weaker change in these characteristics, albeit not linearly. As observed in Table 1, Tco199 generally exhibits a larger difference between the two runs when compared to Tco319 in all characteristics, excluding the block's average size.

To assess the robustness of this result, different overlap and PV anomaly thresholds were tested (not shown). For Tco639, blocking intensity and average size were significant for all overlap values below 0.7 and 0.6 at PV thresholds of -1.2PVU and -1.3PVU respectively. However, blocking duration and the number of blocks detected showed strongest significance between 0.4 to 0.5 overlap for both PV anomaly thresholds. This sensitivity is likely due to merging and splitting events, which simultaneously alter the block's life-cycle and the number of individual blocks detected (Hauser et al., 2023). The change in sign was consistent across all threshold values. While air-sea interactions are suspected to help maintain blocks, this result is less robust than blocking size and intensity. Analysing lower resolutions shows a noisier signal. Although occasionally exhibiting significant signals for block intensity and average size, Tco199 generally exhibits a larger difference between the two runs when compared to Tco319. Neither lower resolution run exhibits significant signals for duration or the number of individual blocks detected.

4 Conclusions

In this study, the impact of suppressing Gulf Stream surface latent heat flux on atmospheric blocking was analysed using a coupled ensemble reforecast on the ECMWF IFS. When this air-sea interaction was suppressed:

1. Atmospheric blocking frequency reduced over the majority of the Northern Hemisphere by up to 30%.
2. The duration, average size, and intensity of atmospheric blocks decreased by approximately 6.4%, 11.5%, and 0.35%, respectively. Additionally, a 16.5% increase in the number of individual blocks detected per forecast was observed.
3. Faster eastward-propagating Rossby waves with larger zonal wave numbers were evident.
4. Resolutions lower than Tco639 ($\sim$18km) exhibited a weaker, non-significant change in block duration, average size, and the number of individual blocks detected per forecast. However, a reduction in blocking frequency and intensity was seen across all resolutions.

We have investigated the effects of air-sea interactions, specifically the influence of the Gulf Stream's surface latent heat flux, on atmospheric blocking. This experiment highlights the significant role that air-sea interactions play in modulating the strength of atmospheric blocks and their potential impacts, both locally and remotely. However, the underlying mechanisms of this process has yet to be understood. A theory proposed by Mathews and Czaja (2024) suggests that air-sea interactions may diabatically influence boundary layer air, which is subsequently transported to the block via warm conveyor belts, altering the quality and quantity of its negative PV anomalies. Ultimately, further research is needed to fully comprehend this process, including its seasonality and robustness across different models.

Appendix A Open Research

Spectral analysis calculations were computed following Randel and Held (1991) using code from Jiménez-Esteve et al. (2022) which is available at `https://github.com/bernatj/paper_GRL_phase_locked_circumglobal_heat_extremes`.

Atmospheric blocks were detected following Schwierz et al. (2004) using the Steinfeld (2020) algorithm, which is available at `https://github.com/steidani/ConTrack`.

Copernicus Climate Change Service (C3S) (2017): ERA5: Fifth generation of ECMWF atmospheric reanalyses of the global climate. Copernicus Climate Change Service Climate Data Store (CDS), date of access. `https://cds.climate.copernicus.eu/cdsapp#!/dataset/reanalysis-era5-pressure-levels?tab=overview`

Acknowledgments

References

Bouillon, S., Maqueda, M. A. M., Legat, V., & Fichefet, T. (2009). An elastic–viscous–plastic sea ice model formulated on arakawa b and c grids. *Ocean Modelling*, *27*(3-4), 174–184.

Coumou, D., Petoukhov, V., Rahmstorf, S., Petri, S., & Schellnhuber, H. J. (2014). Quasi-resonant circulation regimes and hemispheric synchronization of extreme weather in boreal summer. *Proceedings of the National Academy of Sciences*, *111*(34), 12331–12336.

de Rosnay, P., Browne, P., de Boisséson, E., Fairbairn, D., Hirahara, Y., Ochi, K., ... others (2022). Coupled data assimilation at ecmwf: Current status, challenges and future developments. *Quarterly Journal of the Royal Meteorological Society*, *148*(747), 2672–2702.

ECMWF. (2021, 09/2021). Ifs documentation cy47r3 - part iv physical processes. Author. Retrieved from `https://www.ecmwf.int/node/20198` doi: 10.21957/eyrpir4vj

ECMWF. (2023). *Available at:*. `https://www.ecmwf.int/en/publications/ifs-documentation`.

Fichefet, T., & Maqueda, M. M. (1997). Sensitivity of a global sea ice model to the treatment of ice thermodynamics and dynamics. *Journal of Geophysical Research: Oceans*, *102*(C6), 12609–12646.

Grams, C. M., Magnusson, L., & Madonna, E. (2018). An atmospheric dynamics perspective on the amplification and propagation of forecast error in numerical weather prediction models: A case study. *Quarterly Journal of the Royal Meteorological Society*, *144*(717), 2577–2591.

Hauser, S., Teubler, F., Riemer, M., Knippertz, P., & Grams, C. M. (2023). Towards a holistic understanding of blocked regime dynamics through a combination of complementary diagnostic perspectives. *Weather and Climate Dynamics*, *4*(2), 399–425.

He, Y., Zhu, X., Sheng, Z., & He, M. (2023). Resonant waves play an important role in the increasing heat waves in northern hemisphere mid-latitudes under global warming. *Geophysical Research Letters*, *50*(14), e2023GL104839.

Hersbach, H., Bell, B., Berrisford, P., Hirahara, S., Horányi, A., Muñoz-Sabater, J., ... others (2020). The era5 global reanalysis. *Quarterly Journal of the Royal Meteorological Society*, *146*(730), 1999–2049.

Hewitt, H. T., Bell, M. J., Chassignet, E. P., Czaja, A., Ferreira, D., Griffies, S. M.,

... Roberts, M. J. (2017). Will high-resolution global ocean models benefit coupled predictions on short-range to climate timescales? *Ocean Modelling*, *120*, 120–136.

Jiménez-Esteve, B., Kornhuber, K., & Domeisen, D. (2022). Heat extremes driven by amplification of phase-locked circumglobal waves forced by topography in an idealized atmospheric model. *Geophysical Research Letters*, *49*(21), e2021GL096337.

Madec, G., Bourdallé-Badie, R., Bouttier, P.-A., Bricaud, C., Bruciaferri, D., Calvert, D., ... others (2017). Nemo ocean engine.

Mathews, J., & Czaja, A. (2024). Oceanic maintenance of atmospheric blocking in wintertime in the north atlantic.

Paolini, L. F., Bellucci, A., Ruggieri, P., Athanasiadis, P., & Gualdi, S. (2021). *Atmospheric response to gulf stream sst front shifting: impact of horizontal resolution in an ensemble of global climate models* (Tech. Rep.). Copernicus Meetings.

Pfahl, S., Schwierz, C., Croci-Maspoli, M., Grams, C. M., & Wernli, H. (2015). Importance of latent heat release in ascending air streams for atmospheric blocking. *Nature Geoscience*, *8*(8), 610–614.

Pfahl, S., & Wernli, H. (2012). Quantifying the relevance of atmospheric blocking for co-located temperature extremes in the northern hemisphere on (sub-) daily time scales. *Geophysical Research Letters*, *39*(12).

Randel, W. J., & Held, I. m. (1991). Phase speed spectra of transient eddy fluxes and critical layer absorption. *Journal of the atmospheric sciences*, *48*(5), 688–697.

Riboldi, J., Lott, F., d'Andrea, F., & Rivière, G. (2020). On the linkage between rossby wave phase speed, atmospheric blocking, and arctic amplification. *Geophysical Research Letters*, *47*(19), e2020GL087796.

Schwierz, C., Croci-Maspoli, M., & Davies, H. (2004). Perspicacious indicators of atmospheric blocking. *Geophysical research letters*, *31*(6).

Steinfeld, D. (2020). *Contrack - contour tracking.* https://github.com/steidani/ConTrack. GitHub.

Steinfeld, D., Boettcher, M., Forbes, R., & Pfahl, S. (2020). The sensitivity of atmospheric blocking to upstream latent heating–numerical experiments. *Weather and Climate Dynamics*, *1*(2), 405–426.

Wenta, M., Grams, C. M., Papritz, L., & Federer, M. (2024). Linking gulf stream air–sea interactions to the exceptional blocking episode in february 2019: a lagrangian perspective. *Weather and Climate Dynamics*, *5*(1), 181–209.

Yamamoto, A., Nonaka, M., Martineau, P., Yamazaki, A., Kwon, Y.-O., Nakamura, H., & Taguchi, B. (2021). Oceanic moisture sources contributing to wintertime euro-atlantic blocking. *Weather and Climate Dynamics*, *2*(3).

Zuo, H., Balmaseda, M. A., Tietsche, S., Mogensen, K., & Mayer, M. (2019). The ecmwf operational ensemble reanalysis–analysis system for ocean and sea ice: a description of the system and assessment. *Ocean science*, *15*(3), 779–808.